A Dual-Frequency WPT Based on Multilayer Self-Decoupled Compact Coil and Dual *CLCL* Hybrid Compensation Topology

Zhongyu Dai, *Member, IEEE*, and Junhua Wang, *Member, IEEE*

***Abstract*—This article proposes a dual-frequency wireless power transfer (WPT) with dual *CLCL* hybrid compensation topology and multilayer self-decoupled compact coils (MLSDCCs). It extends the transmission distance corresponding to stable high transmission power and efficiency. Based on the parameter constraints of compensation capacitances and inductances, *CLCL* hybrid compensation topology realizes simultaneous resonance at fundamental and third harmonic frequencies. A typical inverter can meet the requirements of dual-frequency WPT without complex control or more number and improve the utilization rate of square voltage. According to interleaving and rotary stacking of unipolar and bipolar coils in MLSDCCs, the couplings between layers and unnecessary couplings of magnetic coupling mechanism (MCM) are eliminated. Only the main couplings for power transmission are retained and the volume of MCM is reduced. Finally, a 1 kW experimental platform is built. Compared with the typical single-frequency WPT, the maximum transmission power is increased by 2.8%, while the maximum transmission efficiency is only reduced by 0.53%. The main advantage is that the transmission distance corresponding to continuous high-power transmission (in the range of 95%–100% maximum receiving power) is increased by 2.75 times. When the lateral offset distance of the *Y*-axis is one-sixth of the coil side length, the transmission efficiency decreases by only 1.47%.**

***Index Terms*—*CLCL* hybrid compensation topology, dual-frequency, self-decoupling, wireless power transfer (WPT).**

I. Introduction

WIRELESS power transfer (WPT) technology has developed rapidly in recent years and has been tentatively applied to many fields [1]. Some low-power WPT devices have been sold in the market, such as wireless phone charger [2]. High-power WPT also has many applications [3]. Especially with the promotion and development of electric vehicles (EVs) in recent years, EV wireless charging has become a typical representative application [4]. Compared with fuel vehicles, EVs still have obvious disadvantages in time-consuming energy replenishment (fuel vehicle refueling and EV charging). To shorten the charging time of EVs, high charging power is the most direct and effective way [5], [6].

The performance of WPT (including transmission efficiency, transmission power, etc.) is closely related to mutual inductance, that is, it is sensitive to transmission distance [7]. The maximum transmission power is obtained at a specific transmission distance known as critical coupling or critical distance [8]. In practical application, the transmission distance of each charging is inevitably different. For example, the ground clearance of EV changes due to different load weights. The variety of transmission distance will lead to the change of mutual inductance, which further affects the power that the receiver can obtain [9].

To ensure stable receiving power, the typical method used is to increase the total power capacity of WPT and then adjust the transmission power according to the change of transmission distance (or mutual inductance). Yang *et al.* [10] demonstrate a T-series compensation topology to guarantee relatively stable current output with various transmission distances. In [11], a neural algorithm is adopted to predict the change of transmission distance. And then the transmission power is adjusted to keep constant the secondary current. In [12], the zero-phase-angle tracking control and phase-shift control are used to hold the stable output voltage with the change of mutual inductance. Zhang *et al.* [13] show an adjustable matrix in the transmitter to overcome the variation of mutual inductance and maintain a stable receiving power. For these published methods, the accuracy of mutual inductance prediction algorithms is not very high. When the transmission distance changes rapidly, the prediction accuracy is lower, and the transmission power regulation strategy is difficult to synchronize. Moreover, the power capacity of WPT is closely related to the variation range of transmission distance corresponding to the stable secondary power. The larger the capacity, the wider the range. But higher power capacity requires materials and equipment with higher voltage and current withstand [14].

When the maximum transmission power of WPT is obtained, the mutual inductance corresponding to different resonance frequencies is various [15], [9], as shown in Fig. 1. That is, each resonance frequency will obtain the maximum transmission

Manuscript received 4 February 2022; revised 10 April 2022 and 16 May 2022; accepted 14 June 2022. Date of publication 16 June 2022; date of current version 26 July 2022. This work was supported by the Fundamental Research Funds for the Central Universities under Grant 2042021kf0012. Recommended for publication by Associate Editor A. Kuperman. *(Corresponding author: Junhua Wang.)*

The authors are with the School of Electrical Engineering and Automation, State Key Laboratory of Water Resources and Hydropower Engineering Science, Wuhan University, Wuhan 430072, China (e-mail: zhongyudai@whu.edu.cn; junhuawang@whu.edu.cn).

Color versions of one or more figures in this article are available at https://doi.org/10.1109/TPEL.2022.3183861.

Digital Object Identifier 10.1109/TPEL.2022.3183861

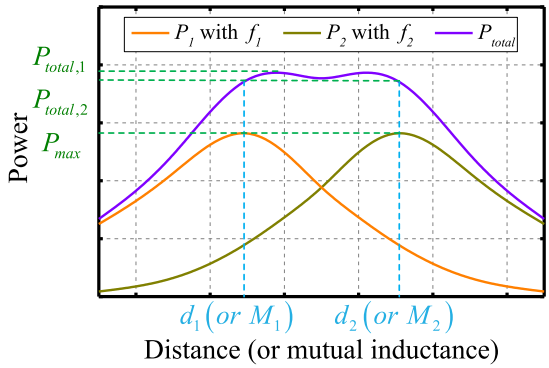

Fig. 1. Transmission power varying with distance (or mutual inductance).

power at a unique critical transmission distance. Based on the superposition law, if a WPT system has multiple resonance frequencies for power transmission at the same time, the total transmission is the sum of that corresponding to each frequency theoretically [16]. High-power transmission can be achieved in a wide range of transmission distance.

Mei *et al.* [17] show a multifrequency WPT with multiple inverters. Each inverter drives one transmitting coil by different frequencies. A relay coil is used to couple the power with various frequencies, which is received by different loads finally [16]. Multifrequency WPT with multiple inverters is most used in the simultaneous wireless power and data transfer system [18]. The advantage of this scheme is that the control of each inverter is simple. But more than one inverter is needed. To reduce the number, multifrequency WPT with a single inverter is proposed. The control algorithm of the inverter is compiled based on the characteristics of multifrequency waveform superposition [19], [20]. The typical superposition is the first and second harmonic wave [21]. The control algorithm is complex, and the switch tubes of inverter with shorter switching time are needed.

If the compensation topology has only one resonant frequency, the impedance of magnetic coupling mechanism (MCM) at nonresonant frequency is very large. This will limit the transmission power capacity at nonresonant frequencies as well as the total transmission power. Simultaneous resonance of multiple frequencies is a basic requirement for compensation topology design of dual-frequency WPT. For series, parallel, and *LCC* topologies, there is only one resonant frequency due to the fixed structure and parameters [22]–[24]. The capacitance in dynamic compensation topology is adjustable [25]. Various capacitances correspond to different resonant frequencies. The switchable compensation topology forms different structures through switches, and the resonant frequency can also be adjusted [26]. The essence of multifrequency of dynamic compensation and switchable compensation is time-sharing single frequency, which cannot realize multifrequency resonance at the same time.

Thus, how to simplify the control algorithm and meet the resonance requirements at all frequencies are important to improve the multifrequency WPT with one inverter. Based on the analysis of the above methods, a dual-frequency WPT is proposed in this article to solve the following problems.

1) Based on the equivalent characteristics of *LC* resonant circuit [27], [28], a dual *CLCL* hybrid compensation topology is designed, which simultaneously satisfies the fundamental and third harmonic resonance conditions to improve the utilization of square voltage and simplify the control of inverter.
2) According to the magnetic field distribution of unipolar and bipolar coils [29], [30], a multilayer self-decoupled compact coil (MLSDCC) is constructed by crossover and rotation to meet the compensation constraints, reduce the volume of MCM, and obtain self-decoupling.

II. Overview of the System

Fig. 2(a) shows a dual-frequency WPT system, mainly including dc source, primary inverter, MCM with dual *CLCL* hybrid compensation topology, secondary rectifier, and load. The dc voltage is converted into square voltage through a inverter. It satisfies

$$U_{\text{square}} = U_{\text{DC}} \tag{1}$$

where U_{DC} and U_{square} are the amplitude of dc voltage and square voltage, respectively.

For the standard square wave, Fourier decomposition is used

$$U_{\text{square}}(t) = \frac{4}{\pi} U_{\text{DC}} \sum_{n=1}^{\infty} \frac{\sin(2n-1)\omega t}{2n-1} \tag{2}$$

where $n = 1, 2, 3, \ldots$ is the positive integer, and $\omega = 2\pi/T$ is the angular frequency.

The square voltage can be decomposed into fundamental and multiple harmonic voltages. If resonance frequencies of dual-frequency WPT happen to be in the sine frequency of the square voltage after Fourier decomposition, a common inverter can meet dual-frequency resonance without complicated control algorithms. The proportion of harmonic content higher than the fifth order is relatively low. When only the fundamental, third, and fifth harmonics are retained, the decomposition and superposition diagrams of each harmonic, as shown in Fig. 3, can be obtained. The more harmonics the vector superimposes, the closer it is to the square wave. The waveform composed of the fundamental, third, and fifth harmonic voltages is very close to a square wave. Based on this superimposed voltage, it is calculated that the proportion of fundamental voltage is 65.22% and that of the third and fifth harmonic are 21.74% and 13.04%, respectively. In a typical WPT, resonance is usually matched based on the fundamental frequency. Only the fundamental voltage is used for power transmission. The utilization rate is only 65.22%. If both fundamental and third harmonic voltage are used, the utilization rate increased to 86.96%. When the first and third harmonic voltages are used at the same time, the withstand voltage of the inverter will not change.

The MCM must be able to resonate at both the first and third frequency so that the fundamental and third harmonic voltages can be simultaneously used for power transmission. The dual-frequency WPT with dual *CLCL* hybrid compensation topology

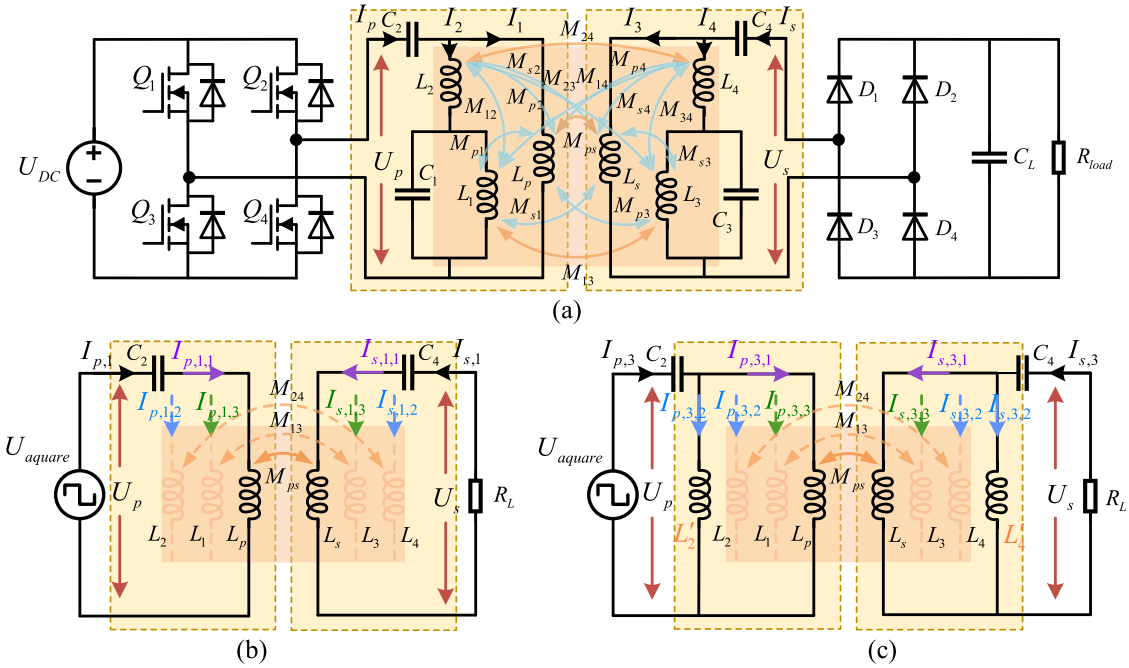

Fig. 2. Dual-frequency WPT with a dual *CLCL* hybrid compensation topology. (a) Overall system structure. (b) Equivalent SS compensation topology. (c) Equivalent dual *LC* compensation topology.

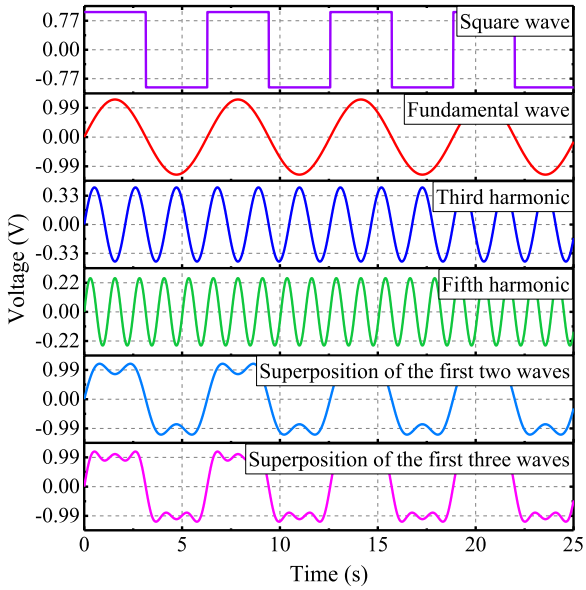

Fig. 3. Fundamental, third, and fifth harmonic of a square wave and their superimposed wave. The period of the square wave is $T = 2\pi$, the angular frequency is $\omega = 2\pi/T = 1$, and the amplitude is $A_{\max} = 1$.

is designed, as shown in Fig. 2(a), where

$$R_L = \left(\frac{2\sqrt{2}}{\pi}\right)^2 R_{\text{load}}. \tag{3}$$

When the resonant frequency is the first frequency f_1, the compensation capacitances C_1, C_2, C_3, and C_4 and coil inductances L_1, L_p, L_3, and L_s in MCM satisfy

$$\omega_1 = 2\pi f_1 = \sqrt{\frac{1}{C_1 L_1}} = \sqrt{\frac{1}{C_2 L_p}} = \sqrt{\frac{1}{C_3 L_3}} = \sqrt{\frac{1}{C_4 L_s}}. \tag{4}$$

The two parallel *LC* resonant circuits composed of C_1, L_1, C_3, and L_3 are equivalent to open circuit. The equivalent circuit is shown in Fig. 2(b), which is a WPT with SS compensation topology.

When the resonant is achieved in the third frequency f_3, the resonant angular frequency is $\omega_3 = 2\pi f_3$. The two hybrid *CLCL* circuits are composed of C_1, L_1, and L_2, and C_3, L_3, and L_4 are equivalent to the inductances of L_2' and L_4'. Fig. 2(c) shows the equivalent circuit. It is a dual *LC* compensation topology. The compensation capacitances C_1, C_2, C_3, and C_4 and coil inductances L_1, L_2, L_3, L_4, L_p, and L_s meet

$$\begin{cases} \omega_3 L'_2 = \omega_3 L_1 \parallel \left(-\frac{1}{\omega_3 C_1}\right) + \omega_3 L_2 \\ \omega_3 L'_4 = \omega_3 L_3 \parallel \left(-\frac{1}{\omega_3 C_3}\right) + \omega_3 L_4 \\ \omega_3 L_p \parallel \omega_3 L'_2 - \frac{1}{\omega_3 C_2} = 0 \\ \omega_3 L_s \parallel \omega_3 L'_4 - \frac{1}{\omega_3 C_4} = 0. \end{cases} \tag{5}$$

For the MCM with a dual *CLCL* hybrid compensation topology, inductances L_1, L_2, L_3, and L_4 are integrated into coils, which can reduce the volume of compensation structures and broaden power transmission channels. Fig. 4 shows the tensile decomposition diagram of MCM composed of MLSDCCs. The compensating coils undertake a part of power transmission, while others are used for inductances. Multiple cross coupling between coils is inevitable in the MCM, including interlayer

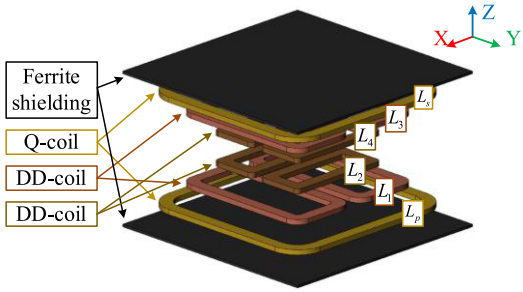

Fig. 4. Tensile decomposition diagram of MCM composed of MLSDCCs.

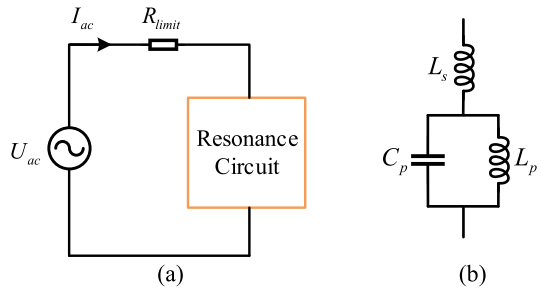

Fig. 5. Impedance characterization analysis of resonant topologies. (a) Analytical circuit model. (b) Simplest *LCL* hybrid resonance topology.

couplings and spatial couplings. Some couplings M_{ps}, M_{13}, and M_{24} form the main power transmission channels, which are necessary and need to be strengthened. Some couplings M_{s1}, M_{s2}, M_{p3}, M_{p4}, M_{14}, and M_{23} can promote power transmission. But in dual-frequency WPT, they will lead to more complex relationship and increase the difficulty of resonance matching. They are usually avoided or decoupled in the design of MCM. Other couplings M_{p1}, M_{p2}, M_{12}, M_{34}, M_{s3}, and M_{s4} will complicate the relationship, have no effect on power transmission, and will increase loss, which should be eliminated.

Based on the above analysis of dual-frequency WPT, to improve the utilization rate of square voltage and the tolerance of transmission power to distance, the following requirements in MCM design should be met.

1) The *CLCL* hybrid compensation topology can reach simultaneous resonances at the first and third harmonic frequencies to realize the dual-frequency magnetic resonance.
2) Coils of MCM are designed into integrated structures to reduce the volume. The inductances of integrated coils meet the requirements of the dual *CLCL* hybrid compensation topology.
3) Only the mutual inductances of the main power transmission channels (M_{ps}, M_{13}, and M_{24}) are retained, and the other mutual inductances should be self-decoupled or eliminated.

III. Compensation Topology of Dual-Frequency Resonance

A. Characteristics of Resonant Circuit

The equivalent characteristic of *LC* resonant circuit is the theoretical basis for resonance compensation. Multiple resonance frequencies are obtained by hybrid connection of capacitances and inductances. The more complex the structure is, the more number of resonant frequencies may be obtained. The multifrequency resonance compensation topology in [31] is only a local resonance, satisfying $f_1 = 1/2\pi\sqrt{L_1C_2}$ and $f_2 = 1/2\pi\sqrt{LC_1}$. Not MCM can achieve resonance at frequencies f_1 and f_2, that is, the reactance of MCM is $X_{\text{MCM}-f_1} \neq 0$, and $X_{\text{MCM}-f_2} \neq 0$. Nonzero resonant reactance will reduce the transmission power. Therefore, it is necessary to design a compensation topology to meet $X_{\text{MCM}-f_1} = 0$ and $X_{\text{MCM}-f_2} = 0$ at the same time.

To analyze the impedance characteristics of *LC* parallel, *LC* series, and the simplest *LCL* hybrid resonant circuits varying with frequency, the circuit model, as shown in Fig. 5, is constructed

$$I_{\text{ac}} = \frac{U_{\text{ac}}}{R_{\text{limit}} + jX_{LC}} = \frac{U_{\text{ac}}}{Z_{LC}} \tag{6}$$

where U_{ac} is the ac source, whose amplitude remains unchanged, R_{limit} is the current limiting resistance, X_{LC} is the reactance of the resonant circuit, and $Z_{LC} = R_{\text{limit}} + jX_{LC}$ is the impedance of the circuit.

Fig. 6 shows the variation of impedance with frequency. When the change trend of impedance amplitude with frequency reverses, the phase of impedance is 0. With the increase of frequency, the impedance amplitude of *LC* parallel first increases and then decreases, while *LC* series exhibits an opposite changing. The frequency corresponding to the inflection point of impedance amplitude is the resonant frequency f_0. When *LC* parallel is in the resonant state $\omega_0 = 2\pi f_0$, the currents flowing through the inductance and capacitance are equal and their directions are opposite. *LC* parallel can be regarded as an open circuit, and the equivalent impedance of the circuit is infinite, as shown in Fig. 6(a). While *LC* parallel is equivalent to a short circuit in resonance frequency f_0, whose impedance is $Z_{LC} = R_{\text{limit}}$. In Fig. 6, if the phase angle of impedance is positive, the reactance X_{LC} is inductive. When the reactance X_{LC} is capacitive, the phase angle is less than 0. The positive and negative transformation also occurs at the resonant frequency f_0. The adjustment of frequency can change both the values and properties of impedance.

The simplest *LCL* hybrid resonant circuit is shown in Fig. 5(b). The variation of its equivalent impedance and phase angle covers the law of *LC* parallel and series changing with frequency, as shown in Fig. 6(c). There are two resonance frequencies f_{01} and f_{02}. Resonant frequencies are also the inflection points of impedance amplitude and properties. When the frequency of *LCL* hybrid resonant circuit satisfies $f_{01} < f_{\text{source}} < f_{02}$, the equivalent reactance X_{LC} is capacitive. It is inductive with the frequency range of $f_{01} > f_{\text{source}}$ and $f_{\text{source}} > f_{02}$.

B. Dual-Frequency Resonance Constraints of MCM With CLCL Hybrid Compensation Topology

To improve the transmission performance of WPT, capacitances and inductances in compensation topology are matched

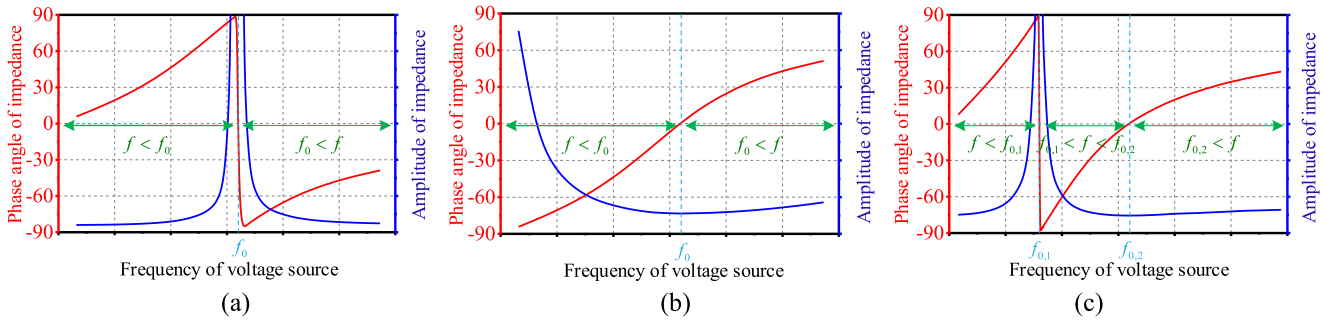

Fig. 6. Impedance of three resonant topologies varying with frequency. (a) *LC* parallel resonance. (b) *LC* series resonance. (c) *LCL* hybrid resonance.

by ideal resonance. For the dual-frequency WPT, as shown in Fig. 2, the *LCL* hybrid resonant circuit needs to be equivalent to an open circuit at the fundamental frequency f_1 and meets (4). At the third harmonic frequency f_3, it should be equivalent to the inductances L_2' and L_4' in (5). The fundamental angular frequency and the third harmonic angular frequency meet

$$3\omega_1 = \omega_3. \tag{7}$$

Combing with (4) and (7), the further simplification of (5) can be obtained

$$\begin{cases} L'_2 = L_2 - \frac{L_1}{8} > 0 \\ L'_4 = L_4 - \frac{L_3}{8} > 0 \\ 8L_2 = L_p + L_1 \\ 8L_4 = L_s + L_3. \end{cases} \tag{8}$$

Equation (8) represents the constraints of inductances in the MCM with dual *CLCL* hybrid compensation topology, which is also the restriction for the parameters of MLSDCCs. If the transmitting and receiving coils are the same structure, the compensation capacitances meet

$$\begin{cases} C_1 = C_3 = \frac{1}{\omega_1^2 L_1} = \frac{9}{\omega_3^2 L_3} \\ C_2 = C_4 = \frac{1}{\omega_1^2 L_p} = \frac{9}{\omega_3^2 L_s}. \end{cases} \tag{9}$$

When the parameters of *CLCL* hybrid compensation topology of MCM are selected, the constraints of (8) and (9) should be followed to meet the dual-frequency WPT with simultaneous resonance of the first and third harmonic frequencies. Standard CBB capacitors are combined in series and parallel to form capacitor banks to meet the requirements. The compensation inductances are the inductances of each subcoils in MLSDCCs.

IV. Integration Design of Coil

A. Magnetic Field Properties of Coils

According to the number of magnetic field directions on one side, coils can be divided into unipolar and bipolar, as shown in Fig. 7. Q coils are typically unipolar, and the magnetic field passing through the coil has only one direction. Fig. 7(b) shows a bipolar coil (also known as DD coil), which can be regarded as two Q subcoils in the same plane. The winding directions of the two Q subcoils are opposite. MCM models composed of Q and DD coils are established. Their magnetic field distribution is analyzed, as shown in Fig. 8. Ferrite is used to optimize MCM to restrict the magnetic field and improve the transmission performance. The outer length and turns of Q and DD coils are the same. The transmission distance between the transmitting coil and receiving coil is half of the side length.

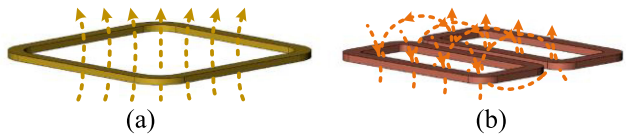

Fig. 7. Typical coil structures of different polarities. (a) Unipolar coil. (b) Bipolar coil.

The magnetic field intensity of coils varying with distance along the selected paths is shown in Fig. 9. Fig. 10 shows the relative spatial relationship between the selected paths and the coils. Paths 2# and 3# are symmetrical. From Fig. 9, the variation of magnetic field intensity on these two paths is the same. For coils without ferrite, as shown in Fig. 9(a), the magnetic field intensity on both sides of coils changes symmetrically. d_A is the position of coils. The magnetic field intensity of coils with ferrite on the side without ferrite is significantly higher than that on the other side, as shown in Fig. 9(b). Compared with coils without ferrite, coils with ferrite have higher magnetic field strength for power transmission and lower that in magnetic leakage area. It verifies the function of ferrite.

From Fig. 9, the magnetic field of DD coil is stronger in the area close to the coil. As the distance from the coil increases, the magnetic field of DD coils decreases faster. After the positions d_B and d_C, the magnetic field strength of Q coils with and without ferrite will be higher than that of DD coils. Fig. 11 shows mutual inductance varying with transmission distance, which has the same change rule. These implies that Q coils are more suitable for long-distance WPT, while DD coils benefit short transmission distance.

B. MLSDCC

The essence of decoupling between coils is that the flux of mutual linkage between coils is 0. Combined with the magnetic field distribution of unipolar and bipolar coils in Fig. 8, two self-decoupled integrated coils, as shown in Fig. 12, are designed.

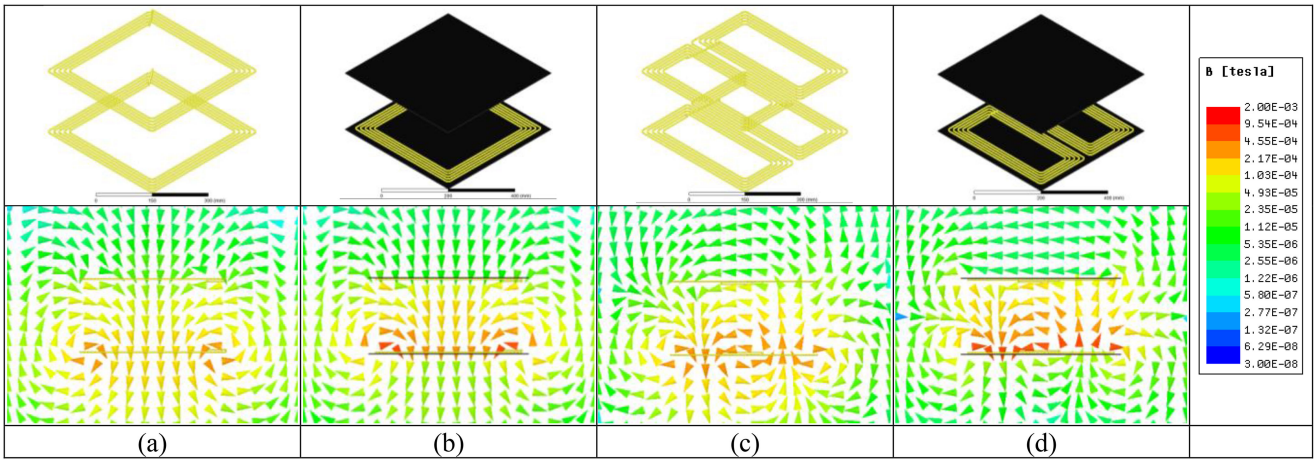

Fig. 8. Magnetic field distribution of MCMs. (a) Q coils. (b) Q coils with ferrite. (c) DD coils. (d) DD coils with ferrite.

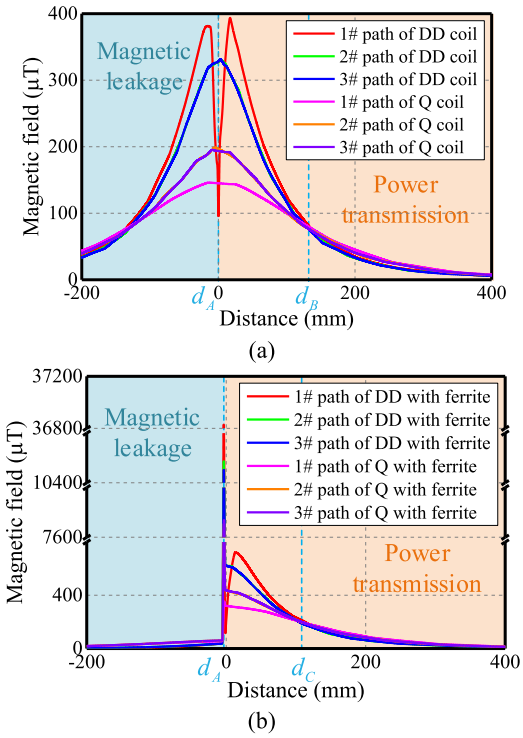

Fig. 9. Magnetic field intensity of coils varying with distance along selected paths. (a) Coils without ferrite. (b) Coils with ferrite.

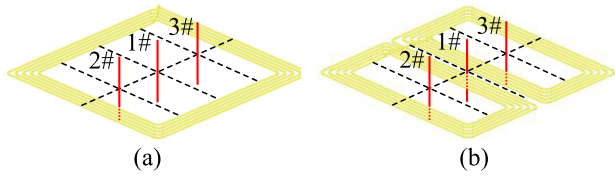

Fig. 10. Relative spatial relationship between the selected paths and coils. (a) Q coil. (b) DD coil.

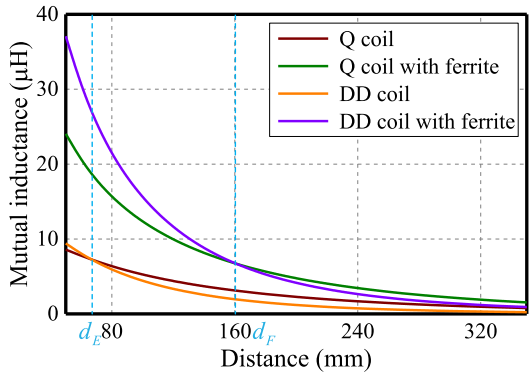

Fig. 11. Mutual inductance varying with transmission distance.

Fig. 12. Self-decoupled integrated coils. (a) DDQ coil. (b) DDDD coil.

The DDQ integrated coil consists of one DD coil and one Q coil. The two coils are parallel and the center point is coaxial, as shown in Fig. 12(a). The amount of magnetic field generated by Q coil passing through the two subcoils of DD coil is the same, which is $\|\phi_{\mathrm{DD}_1,\mathrm{Q}}\| = \|\phi_{\mathrm{DD}_2,\mathrm{Q}}\|$. The winding directions of two subcoils are opposite, that is $\phi_{\mathrm{DD}_1,\mathrm{Q}} = -\phi_{\mathrm{DD}_2,\mathrm{Q}}$. The total linkage flux is $\phi_{\mathrm{DD,Q}} = \phi_{\mathrm{DD}_1,\mathrm{Q}} + \phi_{\mathrm{DD}_2,\mathrm{Q}} = \phi_{\mathrm{DD}_1,\mathrm{Q}} + (-\phi_{\mathrm{DD}_1,\mathrm{Q}}) = 0$. Fig. 12(b) shows a self-decoupled DDDD integrated coil composed of two interlaced DD coils. Two DD coils are rotated 90° relative to each other. From the magnetic field distribution of DD coil and the structure of DDDD coil, the magnetic flux of the mutual linkage of different layers is $\phi_{\mathrm{DD,DD}} = 0$. Both DDQ coil and DDDD coil meet the self-decoupling conditions.

In the WPT with dual *CLCL* hybrid compensation topology, there are three inductances on one side. An MLSDCC is designed, as shown in Fig. 13. Ferrite is added to the opposite side of power transmission. When the transmitting coil and receiving coil are placed in parallel and coaxial, the requirements

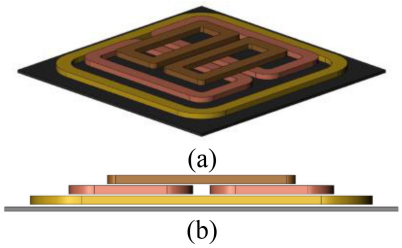

Fig. 13. MLSDCC. (a) Top view. (b) Side view.

set in Fig. 2 can be met. MCM only retains the main mutual inductances M_{ps}, M_{13}, and M_{24s} for power transmission and eliminates other unnecessary couplings.

Not only the self-decoupling should be met in MLSDCC but also the constraints of inductance parameters in dual-frequency resonators. The main coil participates in power transmission at both fundamental and third harmonic frequencies. The coil with the largest mutual inductance shall be selected. According to the structure of MLSDCC, as shown in Fig. 13, the previous analysis of Q coil is the most suitable. For the two compensation inductors in the *CLCL* hybrid compensation topology, (8) must be satisfied, which is $L_2 < L_1$. The outer DD coil is determined as the compensation inductance coil L_2, whose self-inductance is easily to change to meet (8). And its self-inductance is the smallest with the same turns in MLSDCC.

Horizontal offset is inevitable in the practical application of WPT. Both main couplings and cross couplings between the primary and secondary will be affected by horizontal offset. To analyze the influence of horizontal offset, a simulation model of MCM is established according to Fig. 4. The coupling's changing with horizontal offsets is shown in Fig. 14. The representations of mutual inductances in the figure are consistent with that in Section II. According to the structure of MCM composed of MLSDCCs, couplings M_{p1}, M_{p2}, M_{12}, M_{34}, M_{s3}, and M_{s4} between layers inside a coil are eliminated. Main coupling M_{ps} exists between two Q coils, as well as then couplings M_{13} and M_{24} are in DD coils parallel to each other. Couplings M_{s1}, M_{s2}, M_{p3}, and M_{p4} between Q coils and DD coils and couplings M_{14} and M_{23} between staggered DD coils are cross couplings.

Main coupling M_{ps} is the largest, and its changes are the same in the lateral offset of the *X*-axis and *Y*-axis. The variation of couplings M_{13}, M_{s1}, and M_{p3} are greater with the horizontal offset along the *X*-axis, while that of M_{24} M_{s2}, and M_{p4} are the *Y*-axis. Couplings M_{14} and M_{23} are always very small with the horizontal offsets. Compared with the horizontal offset in the *X*-axis, couplings of MCM are more stable in the *Y*-axis. Main couplings M_{ps} and M_{13} are almost unchanged within the range of 50 mm/300 mm $=$ 1/6 of the coil side length.

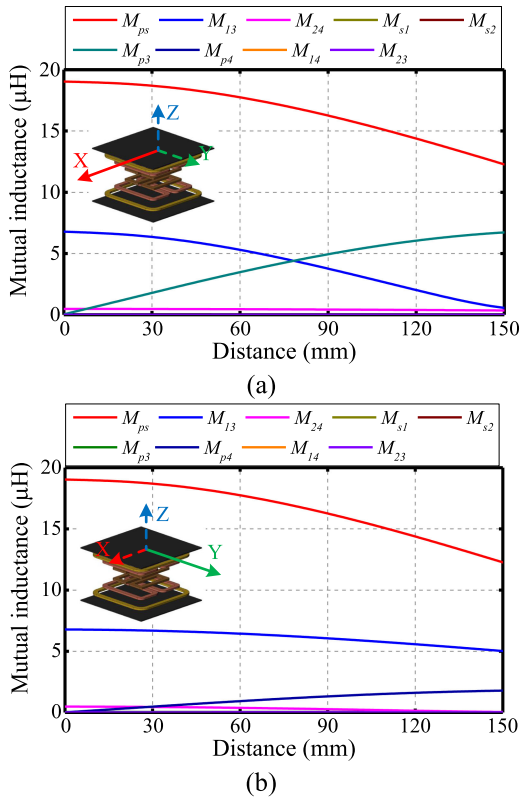

Fig. 14. Couplings varying with horizontal offsets. (a) Horizontal offset in the *X*-axis. (b) Horizontal offset in the *Y*-axis.

TABLE I
PHYSICAL PARAMETERS OF MCM

Parameter		Value
Wire		0.1 *mm* * 300 Litz
Coils L_p and L_s	Type	Q coil
	Length of side	300 *mm*
	Turns	10
Coils L_1 and L_3	Type	DD coil
	Length of short side	120 *mm*
	Length of long side	240 *mm*
	Turns	10
Coils L_2 and L_4	Type	DD coil
	Length of short side	80 *mm*
	Length of long side	160 *mm*
	Turns	6
Ferrite	Type	Square
	Length of side	320 *mm*
	Thickness	5 *mm*

V. EXPERIMENT

An experimental platform is built, as shown in Fig. 15, including dc source (IT8512A), inverter (C3M0065090), MCM (composed of MLSDCCs, ferrite-shielding, and compensation capacitances), rectifier, and electronic load. MCM adopts double *CLCL* hybrid compensation topology proposed above. The fundamental resonance frequency is 95 kHz. The physical and electrical parameters of MCM are shown in Tables I and II. The parameters of MCM correspond to the structure, as shown in Fig. 4. The only difference between the single-frequency and dual-frequency WPT is MCM. The MCM of single-frequency WPT consists of coils L_p and L_s and compensation capacitances

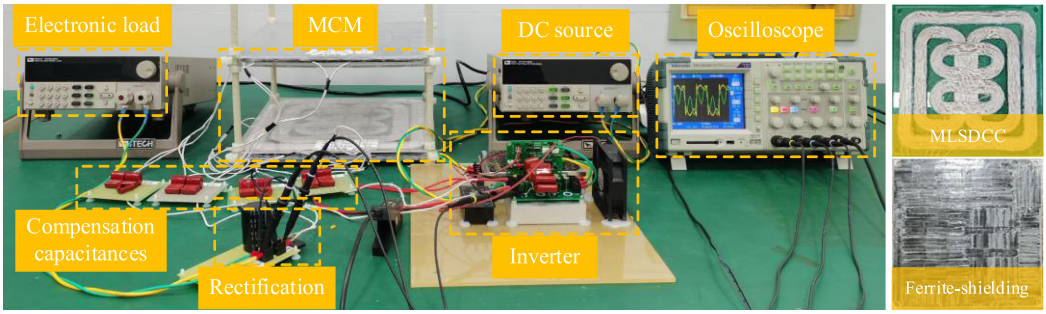

Fig. 15. Experimental platform.

TABLE II
ELECTRICAL PARAMETERS OF MCM

Parameter	Value	Parameter	Value
L_p	98.5 μH	L_s	96.4 μH
L_1	91.0 μH	L_3	94.3 μH
L_2	23.7 μH	L_4	23.8 μH
C_1	29.3 nF	C_3	29.1 nF
C_2	27.7 nF	C_4	28.1 nF

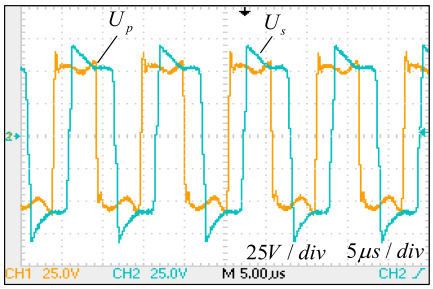

Fig. 16. Input and output voltage of MCM.

C_2 and C_4. Since the coil is manually wound, there are some differences between the transmitting and receiving coils with the same turns and structure. Coils L_p, L_s, L_1, and L_3 are first wound, then the turns of coils L_2 and L_4 are adjusted to meet (8). Compensation capacitance is calculated according to (9). Standard CBB capacitors with 2 kV withstand voltage are combined to be used as compensation capacitances.

Fig. 16 shows the primary and secondary voltage of MCM when the dc voltage is 60 V and the transmission distance is 15 cm. Yellow line means the primary voltage, which is the output voltage of inverter. Cyan line represents the output voltage of MCM. Due to the influence of couplings and dual-frequency resonant, amplitudes fluctuate. The voltages on the primary and secondary sides are similar to square wave, and the frequency is the same as the source. Different from the sinusoidal voltage at receivers of typical single-frequency WPT, the square voltage at the secondary side verifies the theory and design aimed at improving the voltage utilization of inverter. According to the proposed topology in Fig. 2 and the Fourier decomposition of square voltage in Fig. 3, the output voltage is the vector superposition of fundamental and third harmonic voltage. That is, *LC* resonance of the first and third harmonic frequency is realized in MCM at the same time.

The primary and secondary voltage of MCM and current of each coil are shown in Fig. 17. The currents I_p, I_1, I_2, I_s, I_3, and I_4 and voltages U_p and U_s correspond to Fig. 2. Phase-angle differences between the primary voltage U_p and currents I_p and I_1 are 0, while that are nonzero between the secondary voltage and currents. The phase-angle differences of secondary side are caused by many factors, such as handmade difference, cross couplings, compensation capacitances, and so on. Refer to the frequency of voltages U_p and U_s, currents I_1 and I_3 are fundamental frequency f_1, while currents I_2 and I_4 are the third harmonic frequency f_3. Waveforms of all currents are approximately sinusoidal. Current branches I_1 and I_2 are connected in parallel. The difference in frequency of currents I_1 and I_2 under the same voltage indicates that current I_1 is produced by fundamental resonance, while I_2 is mainly generated by the resonance of third harmonic. The variations of currents and voltages at the primary and secondary sides of MCM, as shown in Fig. 17, are almost the same. These verify that the topology of Fig. 2(a) can get resonance at both the first and third harmonic frequencies. According to the characteristics of resonance magnetic coupling WPT, there are at least two power transmission chancels. That is, the designed topology realizes dual-frequency WPT with one typical inverter.

Currents of each coil on the primary and secondary sides of MCM are extracted separately to form Fig. 18. For the topology of Fig. 2, there are $I_p = I_1 + I_2$ and $I_s = I_3 + I_4$ according to Kirchhoff's current law. The current variation, as shown in Fig. 18, also satisfies this law. The amplitude of primary first current is much less than that of the third. One reason is that the ratio of the third voltage to the fundamental voltage is $21.24\%/65.22\% = 32.57\%$. Another reason is that more components are in the path of third harmonic current. The path has greater reactance. The secondary first and third currents are obtained by magnetic field coupling. From Table I, the outer diameter of DD coil is smaller than that of Q coil. When the transmission distance is greater than the critical distance, the coupling of the third harmonic power transmission channels is lower than that of the fundamental resonant. The third current on the secondary side of MCM is less than that of the first current.

To analyze the stability improvement of transmission power and efficiency when the transmission distance changes, the concept of distance-to-diameter ratio (DDR) of stable transmission

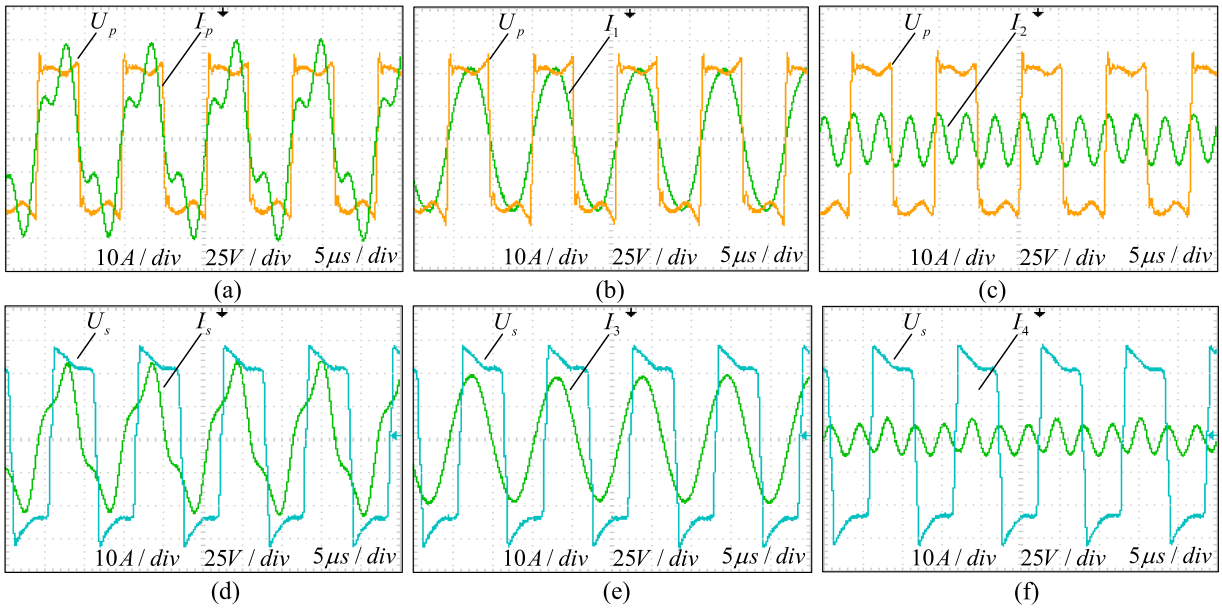

Fig. 17. Primary and secondary voltages of MCM and currents of each coil. (a) Primary voltage U_p and total primary current I_p. (b) Primary voltage U_p and current I_1. (c) Primary voltage U_p and current I_2. (d) Secondary voltage U_s and total secondary current I_s. (e) Secondary voltage U_s and current I_3. (f) Secondary voltage U_s and current I_4.

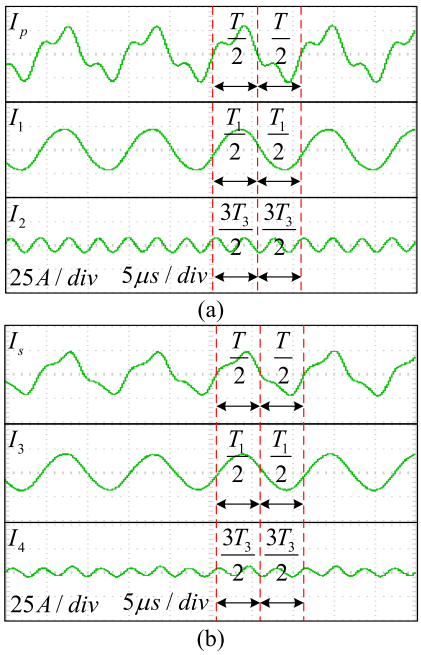

Fig. 18. Currents of each coil. (a) Primary side. (b) Secondary side. T is the period of inverter, and T_1 and T_3 are the period of fundamental and third harmonic frequency.

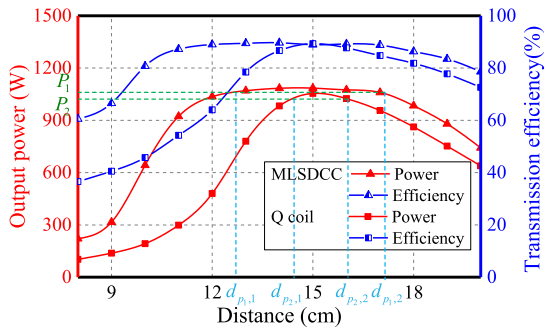

Fig. 19. Transmission power and efficiency varying with transmission distance.

is defined [32] as follows:

$$\mathrm{DDR}_{\mathrm{stable}} = \frac{D_{\mathrm{distance}}}{D_{\mathrm{max}}} \tag{10}$$

where D_{distance} is the transmission distance corresponding to stable power transmission, and D_{max} is the maximum equivalent diameter of coils. For MLSDCCs designed in experiment, $D_{\mathrm{max}} = 2\sqrt{2}\,R_Q = 30\sqrt{2}$ cm.

The transmission power and efficiency changing with the transmission distance of dual-frequency WPT (MLSDCC) and typical single-frequency WPT (Q coil) are shown in Fig. 19. The transmission power is the output power of the dc source, and the receiving power is the output power of rectifier, that is, the power obtained by load. Transmitting efficiency is the ratio of receiving power to transmission power. With the increase of transmission distance, transmission power and efficiency increase first and then decrease. The maximum receiving power of dual-frequency WPT and single-frequency WPT is 1085 and 1054 W. While the maximum transmission efficiency of dual-frequency WPT is 89.33%, which is slightly lower than that of 89.86% of single-frequency WPT. That is, the maximum transmission power is increased by 2.8% and the maximum transmission efficiency is reduced by 0.53%. The stable transmission power selected in this article is the range of 95%–100% maximum receiving power. In Fig. 19, P_1 and P_2 are the 95% maximum receiving power of dual-frequency and single-frequency WPT, which are 1031 and 1001 W. The starting end points of stable power

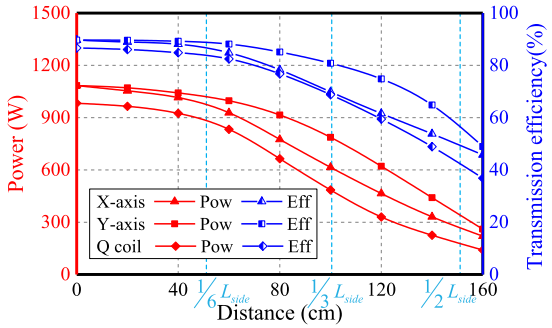

Fig. 20. Transmission power and efficiency varying with horizontal offset. L_{side} is the side length of MLSDCC and Q coil.

transmission corresponding to P_1 and P_2 are $d_{P_1,1} = 12.8$ cm, $d_{P_1,2} = 17.2$ cm, $d_{P_2,1} = 14.5$ cm, and $d_{P_2,2} = 16.1$ cm. Thus, the DDRs of dual-frequency and single-frequency WPT are about $\text{DDR}_{\text{dual}} = (17.2 - 12.8)/30\sqrt{2} = 10.37\%$ and $\text{DDR}_{\text{single}} = (16.1 - 14.5)/30\sqrt{2} = 3.77\%$. The distance of stable transmission is increased by 2.75 times.

The influence of horizontal offset on transmission power and transmission efficiency is shown in Fig. 20. The transmission distance is 15 cm. With the increase of offset distance, transmission power and efficiency continue to decrease. The transmission efficiency and power of Q coil (single-frequency WPT) with lateral offset are always less than that of MLSDCC (dual-frequency WPT). For MLSDCC, the influence of lateral offset in the *X*-axis is more significant. Compared with the reduction rate of transmission efficiency and power caused by the *Y*-axis offset, in the *X*-axis, it is faster when the offset distance is less than $1/3L_{\text{side}}$. This is because M_{13} drops faster in the *X*-axis offset. After the distance is greater than $1/3L_{\text{side}}$, the reduction rate of the *X*-axis is less slow. The reason is the enhancement of cross couplings M_{s1} and M_{p3}. They also undertake a part of power transmission. When the lateral offset distance of the *Y*-axis is $1/6L_{\text{side}}$, the transmission efficiency decreases by only 1.47%, which is consistent with the previous analysis of couplings varying with horizontal offsets. In applications, the *Y*-axis of MCM shall be parallel to the direction prone to lateral offset to maintain the stability of power transmission.

VI. Conclusion

This article presents a dual-frequency WPT. Based on the characteristic of typical *LC* resonant circuits, a *CLCL* hybrid compensation topology is constructed, and the constraints of simultaneous resonance at fundamental and third harmonic frequencies are derived to reduce the requirements for inverter. An MLSDCC is designed to meet the requirements of inductances and reduce the occupation space of coils. Based on the magnetic field distribution of unipolar and bipolar coils, DD coils and Q coils are used to achieve self-decoupling of each layer by rotating and cross arrangement. The unnecessary couplings are eliminated, and only the main couplings for power transmission are retained. *CLCL* hybrid compensation topologies and MLSDCCs jointly realize dual-frequency WPT, whose performances are verified by experiments. The results are consistent with theoretical analysis, which improves the utilization of square voltage. Compared with the typical single-frequency WPT, dual-frequency WPT improves maximum transmission power by 2.8% with 0.53% maximum transmission efficiency reducing. The greatest advantage is that the range of transmission distance corresponding to stable high-power transmission is increased by 2.75 times. In application, the *X*-axis of MCM should avoid being parallel to the direction prone to lateral offset.

References

[1] Z. Zhang, H. Pang, A. Georgiadis, and C. Cecati, "Wireless power transfer—An overview," *IEEE Trans. Ind. Electron.*, vol. 66, no. 2, pp. 1044–1058, Feb. 2019, doi: 10.1109/TIE.2018.2835378.

[2] M. Filipiak, D. Głuchy, and M. Godek, "Analysis of the wireless charging technologies impact on the charging process parameters of mobile devices," *ITM Web Conf.*, vol. 28, 2019, Art. no. 01008, doi: 10.1051/itmconf/20192801008.

[3] Z. Dai, J. Wang, H. Zhou, and H. Huang, "A review on the recent development in the design and optimization of magnetic coupling mechanism of wireless power transmission," *IEEE Syst. J.*, vol. 14, no. 3, pp. 4368–4381, Sep. 2020, doi: 10.1109/JSYST.2020.3004201.

[4] S. Jayalath and A. Khan, "Design, challenges, and trends of inductive power transfer couplers for electric vehicles: A review," *IEEE J. Emerg. Sel. Topics Power Electron.*, vol. 9, no. 5, pp. 6196–6218, Oct. 2021, doi: 10.1109/JESTPE.2020.3042625.

[5] Z. Dai, J. Wang, M. Long, and H. Huang, "A witricity-based high-power device for wireless charging of electric vehicles," *Energies*, vol. 10, no. 3, 2017, Art. no. 323, doi: 10.3390/en10030323.

[6] A. U. Ibrahim, W. Zhong, and M. D. Xu, "A 50-kW three-channel wireless power transfer system with low stray magnetic field," *IEEE Trans. Power Electron.*, vol. 36, no. 9, pp. 9941–9954, Sep. 2021, doi: 10.1109/TPEL.2021.3064373.

[7] A. Kurs, A. Karalis, R. Moffatt, J. D. Joannopoulos, P. Fisher, and M. Soljacic, "Wireless power transfer via strongly coupled magnetic resonances," *Science*, vol. 317, no. 5834, pp. 83–86, 2007, doi: 10.1126/science.1143254.

[8] T. Orekan, P. Zhang, and C. Shih, "Analysis, design, and maximum power-efficiency tracking for undersea wireless power transfer," *IEEE J. Emerg. Sel. Topics Power Electron.*, vol. 6, no. 2, pp. 843–854, Jun. 2018, doi: 10.1109/JESTPE.2017.2735964.

[9] X. Dai, X. Li, Y. Li, and A. P. Hu, "Impedance-matching range extension method for maximum power transfer tracking in IPT system," *IEEE Trans. Power Electron.*, vol. 33, no. 5, pp. 4419–4428, May 2018, doi: 10.1109/TPEL.2017.2716968.

[10] B. Yang *et al.*, "Analysis and design of a T/S compensated IPT system for AGV maintaining stable output current versus air gap and load variations," *IEEE Trans. Power Electron.*, vol. 37, no. 5, pp. 6217–6228, May 2022, doi: 10.1109/TPEL.2021.3135053.

[11] Z. Zhang and W. Yu, "Communication/model-free constant current control for wireless power transfer under disturbances of coupling effect," *IEEE Trans. Ind. Electron.*, vol. 69, no. 5, pp. 4587–4595, May 2022, doi: 10.1109/TIE.2021.3084174.

[12] M. Kim, D.-M. Joo, and B. K. Lee, "Design and control of inductive power transfer system for electric vehicles considering wide variation of output voltage and coupling coefficient," *IEEE Trans. Power Electron.*, vol. 34, no. 2, pp. 1197–1208, Feb. 2019, doi: 10.1109/TPEL.2018.2835161.

[13] K. Zhang, W. Gao, R. Shi, Z. Yan, B. Song, and A. P. Hu, "An impedance matching network tuning method for constant current output under mutual inductance and load variation of IPT system," *IEEE Trans. Power Electron.*, vol. 35, no. 10, pp. 11108–11118, Oct. 2020, doi: 10.1109/TPEL.2020.2978104.

[14] R. Bosshard and J. W. Kolar, "All-SiC 9.5 kW/dm^3 on-board power electronics for 50 kW/85 kHz automotive IPT system," *IEEE J. Emerg. Sel. Topics Power Electron.*, vol. 5, no. 1, pp. 419–431, Mar. 2017, doi: 10.1109/JESTPE.2016.2624285.

[15] Y. Sun, Z.-J. Liao, Z.-H. Ye, C.-S. Tang, and P.-Y. Wang, "Determining the maximum power transfer points for MC-WPT systems with arbitrary number of coils," *IEEE Trans. Power Electron.*, vol. 33, no. 11, pp. 9734–9743, Nov. 2018, doi: 10.1109/TPEL.2018.2799241.

[16] F. Liu, Y. Yang, Z. Ding, X. Chen, and R. M. Kennel, "A multifrequency superposition methodology to achieve high efficiency and targeted power distribution for a multiload MCR WPT system," *IEEE Trans. Power Electron.*, vol. 33, no. 10, pp. 9005–9016, Oct. 2018, doi: 10.1109/TPEL.2017.2784566.

[17] T. Mei, X. Zhang, F. Liu, X. Chen, and R. M. Kennel, "Multi-frequency phase-shifted angle control strategy for a two-phase MCR WPT system with multiple loads to achieve targeted power distribution and stable transmission power," in *Proc. IEEE Appl. Power Electron. Conf. Expo.*, 2019, pp. 3117–3122.

[18] Y. Fan, Y. Sun, X. Dai, Z. Zuo, and A. You, "Simultaneous wireless power transfer and full-duplex communication with a single coupling interface," *IEEE Trans. Power Electron.*, vol. 36, no. 6, pp. 6313–6322, Jun. 2021, doi: 10.1109/TPEL.2020.3035782.

[19] C. Qi, S. Huang, X. Chen, and P. Wang, "Multifrequency modulation to achieve an individual and continuous power distribution for simultaneous MR-WPT system with an inverter," *IEEE Trans. Power Electron.*, vol. 36, no. 11, pp. 12440–12455, Nov. 2021, doi: 10.1109/TPEL.2021.3081931.

[20] W. Liu, K. T. Chau, C. H. T. Lee, C. Jiang, W. Han, and W. H. Lam, "Multi-frequency multi-power one-to-many wireless power transfer system," *IEEE Trans. Magn.*, vol. 55, no. 7, Jul. 2019, Art. no. 8001609, doi: 10.1109/TMAG.2019.2896468.

[21] D. Thenathayalan and J.-H. Park, "Individually regulated multiple-output WPT system with a single PWM and single transformer," *IEEE J. Emerg. Sel. Topics Power Electron.*, vol. 8, no. 4, pp. 3542–3557, Dec. 2020, doi: 10.1109/JESTPE.2019.2925190.

[22] L. Wang, J. Li, H. Chen, and Z. Pan, "Radial-flux rotational wireless power transfer system with rotor state identification," *IEEE Trans. Power Electron.*, vol. 37, no. 5, pp. 6206–6216, May 2022, doi: 10.1109/TPEL.2021.3132702.

[23] M. Ishihara, K. Umetani, and E. Hiraki, "Strategy of topology selection based on quasi-duality between series–series and series–parallel topologies of resonant inductive coupling wireless power transfer systems," *IEEE Trans. Power Electron.*, vol. 35, no. 7, pp. 6785–6798, Jul. 2020, doi: 10.1109/TPEL.2019.2956732.

[24] Y. Chen, H. Zhang, C.-S. Shin, C.-H. Jo, S.-J. Park, and D.-H. Kim, "An efficiency optimization-based asymmetric tuning method of double-sided LCC compensated WPT system for electric vehicles," *IEEE Trans. Power Electron.*, vol. 35, no. 11, pp. 11475–11487, Nov. 2020, doi: 10.1109/TPEL.2020.2984712.

[25] C. S. Wong, M.-C. Wong, L. Cao, and K. H. Loo, "Design of high-efficiency inductive charging system with load-independent output voltage and current tolerant of varying coupling condition," *IEEE Trans. Power Electron.*, vol. 36, no. 12, pp. 13546–13561, Dec. 2021, doi: 10.1109/TPEL.2021.3086858.

[26] H. Li, Y. Yang, J. Chen, J. Xu, M. Liu, and Y. Wong, "A hybrid class-E topology with constant current and constant voltage output for light EVs wireless charging application," *IEEE Trans. Transp. Electrific.*, vol. 7, no. 4, pp. 2168–2180, Dec. 2021, doi: 10.1109/TTE.2021.3083363.

[27] J. Mai, Y. Wang, Y. Yao, and D. Xu, "Analysis and design of high-misalignment-tolerant compensation topologies with constant-current or constant-voltage output for IPT systems," *IEEE Trans. Power Electron.*, vol. 36, no. 3, pp. 2685–2695, Mar. 2021, doi: 10.1109/TPEL.2020.3014687.

[28] G. Ke, Q. Chen, L. Xu, X. Ren, and Z. Zhang, "Analysis and optimization of a double-sided S-LCC hybrid converter for high misalignment tolerance," *IEEE Trans. Ind. Electron.*, vol. 68, no. 6, pp. 4870–4881, Jun. 2021, doi: 10.1109/TIE.2020.2988215.

[29] F. Wen, X. Cheng, Q. Li, W. Zhao, X. Zhu, and Y. Wu, "A strong misalignment tolerance dual-channel coupler for wireless power transfer system," *IEEE Trans. Appl. Supercond.*, vol. 31, no. 8, Nov. 2021, Art. no. 0601005, doi: 10.1109/TASC.2021.3091099.

[30] C. Cai, S. Wu, Z. Zhang, L. Jiang, and S. Yang, "Development of a fit-to-surface and lightweight magnetic coupler for autonomous underwater vehicle wireless charging systems," *IEEE Trans. Power Electron.*, vol. 36, no. 9, pp. 9927–9940, Sep. 2021, doi: 10.1109/TPEL.2021.3064411.

[31] Z. Zhang, X. Li, H. Pang, H. Komurcugil, Z. Liang, and R. Kennel, "Multiple-frequency resonating compensation for multichannel transmission of wireless power transfer," *IEEE Trans. Power Electron.*, vol. 36, no. 5, pp. 5169–5180, May 2021, doi: 10.1109/TPEL.2020.3027916.

[32] Y. Wang, P. Gu, Y. Yao, and D. Xu, "Analysis and design of cubic magnetic coupler for high distance-to-diameter ratio IPT systems," *IEEE Trans. Ind. Electron.*, vol. 69, no. 1, pp. 409–419, Jan. 2022, doi: 10.1109/TIE.2020.3048294.